A Novel Humanized Mouse Model for HIV and Tuberculosis Co-infection Studies

José Alejandro Bohórquez*[1, 2, 3], Sitaramaraju Adduri*[1, 2], Danish Ansari[1, 2, 3], Sahana John[1, 2, 3], Jon Florence[1,2], Omoyeni Adejare[1,2], Gaurav Singh[3], Nagarjun Konduru[1,2], Chinnaswamy Jagannath[4], and Guohua Yi[1, 2, 3#]

1. Department of Cellular and Molecular Biology, The University of Texas Health Science Center at Tyler, Tyler, TX 75708, USA.

2. Center for Biomedical Research, The University of Texas Health Science Center at Tyler, Tyler, TX 75708, USA.

3. Department of Medicine, The University of Texas at Tyler School of Medicine, Tyler, TX 75708, USA.

4. Department of Pathology and Genomic Medicine, Center for Infectious Diseases and Translational Medicine, Houston Methodist Research Institute, Houston, TX, USA

* Authors contributed equally to this work

#Corresponding author. Email: guohua.yi@uthct.edu

Key words

Humanized mouse model, HIV, *Mycobacterium tuberculosis*, NSG-SGM3 mice, HIV/*Mtb*-induced immunopathogenesis, HIV/*Mtb*-differentiated metabolites

ABSTRACT

Tuberculosis (TB), caused by *Mycobacterium tuberculosis* (*Mtb*), continues to be a major public health problem worldwide. The human immunodeficiency virus (HIV) is another equally important life-threatening pathogen. Further, co-infections with HIV and *Mtb* have severe effects in the host, with people infected with HIV being fifteen to twenty-one times more likely to develop active TB. The use of an appropriate animal model for HIV/*Mtb* co-infection that can recapitulate the diversity of the immune response in humans would be a useful tool for conducting basic and translational research in HIV/*Mtb* infections. The present study was focused on developing a humanized mouse model for investigations on HIV-*Mtb* co-infection. Using NSG-SGM3 mice that can engraft human stem cells, our studies showed that they were able to engraft human CD34+ stem cells which then differentiate into a full-lineage of human immune cell subsets. After co-infection with HIV and *Mtb*, these mice showed decrease in CD4+ T cell counts overtime and elevated HIV load in the sera, similar to the infection pattern of humans. Additionally, *Mtb* caused infections in both lungs and spleen, and induced the development of granulomatous lesions in the lungs, detected by CT scan and histopathology. Distinct metabolomic profiles were also observed in the tissues from different mouse groups after co-infections. Our results suggest that the humanized NSG-SGM3 mice are able to recapitulate the effects of HIV and *Mtb* infections and co-infection in the human host at pathological, immunological and metabolism levels, providing a dependable small animal model for studying HIV/*Mtb* co-infection.

INTRODUCTION

Tuberculosis (TB) remains one of the biggest public health problems worldwide, being the second cause of death in mankind in 2022, behind COVID-19 [1]. Over seven million people were newly diagnosed with TB in the past year and around 1.3 million people were killed by this deadly disease. There is a consensus that a quarter of the world population are infected with *Mycobacterium tuberculosis* (*Mtb)*, the causative agent for TB[1]. The majority of *Mtb*-infected individuals remain latently infected without clinical signs (LTBI). However, around 10% of the infected patients will develop active TB, especially in conjunction with immunodeficiency caused by malnutrition, immunosuppressive therapy using steroids, or infection with immunosuppressive pathogens[2]. Among these infection with human immunodeficiency virus (HIV) plays a pivotal role, given that immunosuppression is the hallmark of HIV pathogenesis[3]. HIV is the etiological agent for acquired immunodeficiency syndrome (AIDS), another equally important public health concern responsible for the death of over 40 million people as of 2023[4]. The synergy between HIV and *Mtb* in co-infection has been extensively examined, and compelling evidence showed that HIV exacerbates TB severity, and is the leading cause of death for people infected with *Mtb*[4-6]. This is likely because HIV-induced immunosuppression leads to a disruption of CD4 T cells, the main driver of Th-1 immunity in LTBI patients, resulting in active TB[7].

Non-human primates (NHP) are routinely used as large animal models for HIV/*Mtb* research not only because the monkeys and humans have remarkably similar genomes, physiology, and immune systems, but also because the monkeys can be infected by both *Mtb* and Simian immunodeficiency virus (SIV)[8]. The latter is also a retrovirus and belongs to the same Lentivirus genus as HIV and causes HIV-like infection in NHPs. After co-infection, NHPs also display AIDS-like features as in humans, such as massive reduction of CD4+ T cells and a high viral load in the

sera if without anti-retroviral treatment, as well as chronic immune activation in animals during extended observation [7, 9]. Furthermore, the co-infected monkeys also recapitulate key aspects of human TB infection stages, including latent infection, chronic progressive infection, and acute TB, depending on the route and dose of infection[10-12]. Importantly, *Mtb* latently infected macaques co-infected with SIV results in reproducible LTBI reactivation[13], providing a reliable model for HIV/*Mtb* research. However, NHPs require specialized infrastructure for experimentation and are cost-restrictive, and are not readily available in the majority of animal facilities[14, 15],

The use of other small animal models, such as rodents poses different challenges. Although inbred and genetic knockout mice are easily available, and readily infective using *Mtb*, most strains of mice are not a natural host for HIV, which require human $CD4^+$ T cells to establish infection. Whereas the use of mouse models for *Mtb* research has also been criticized due to their inability to form granulomas which are a hallmark of *Mtb* infection in humans[16], certain mouse strains and infection protocols show the formation of granulomas. [17]. Fortunately, humanized mouse models, the immunodeficient mice that have been reconstituted with a human immune system, appears to be a promising small animal model for HIV and *Mtb* reseach[14, 15, 18, 19]. They have been extensively used for evaluating HIV gene therapy and therapeutics[20, 21], and recently, the NSG (NOD scid gamma)-based humanized BLT mice were developed for analyzing *Mtb* and HIV/*Mtb* co-infections[15, 18, 22]. However, humanized BLT mice need surgical transplantation (under the kidney capsule) of fetal liver, bone marrow and thymus tissues, and restriction of human fetal tissues used for research and the sophisticated surgery has markedly limited the use of this model. In addition, these mice have immature B cells with poor IgG class-switching and poor reconstitution of myeloid lineage of antigen-presenting cells (APCs)[23, 24], posing a challenge for

HIV/*Mtb* research because myeloid cells, especially macrophages, are important targets for both HIV and *Mtb.*

We demonstrate here that these deficiencies can be ameliorated in the newly developed NSG-SGM3 mice, which transgenically express three human cytokine/chemokine genes IL-3, GM-CSF, and KITLG. The expression of these genes improves the differentiation and maturation of the myeloid cells[25-29]. The present study is aimed at establishing a reliable new-generation, humanized mouse model for the HIV/*Mtb* co-infection research. We show that humanized NSG-SGM3 mice can differentiate CD34+ stem cells into a full-lineage of immune cell subsets, including both lymphoid and myeloid lineages. Importantly, we show that HIV/*Mtb* infections are reproducible in these mice with a spectrum of immunological, pathological, and metabolic changes when compared to uninfected mice.

MATERIALS AND METHODS

Bacterial and viral strains

Mtb H37Rv was obtained from BEI Resources (USA) and propagated in the biosafety level 3 (BSL-3) facilities at the University of Texas Health Science Center at Tyler (UTHSCT). It was cultured in 7H9 broth with 10% OADC supplement following standard *Mtb* culture procedures[30]. After 7 days of growth, the bacteria were collected and subjected to sonication three times, at an amplitude of 38%, for 10 seconds/each, with a 5-second interval, followed by low-speed centrifugation (1,100 RPM). Bacteria were diluted to an optical density (OD) value of ≈ 1 in sterile NaCl 0.9% and aliquots were made and frozen at -80 °C to be used as inoculum. Two weeks later, one aliquot was thawed, and the bacterial content was evaluated by plating ten-fold serial dilutions

in 7H10 agar, supplemented with OADC. After 3 weeks of incubation, the colony forming units (CFU) per mL were calculated.

HIV-1 BaL strain was obtained from NIH AIDS Reagent Program, also prepared in the BSL-3 facilities at UTHSCT, following standard procedures [31]. Briefly, frozen human PBMCs (STEMCELL Technologies, Vancouver, Canada) were thawed and seeded in a 75 cm^2 flask at a concentration of 5×10^6 cells/mL in RPMI 1640 media (Corning Inc., Corning, NY) supplemented with 10% fetal bovine serum (FBS), 1% penicillin/streptomycin, 1 µg/ml of PHA and 2 µg/ml polybrene (MilliporeSigma, Burlington, MA). After 3 days of stimulation, 4×10^7 cells were centrifuged and infected with HIV-1 BaL using an MOI (multiplicity of infection) of 0.1 (4×10^6 $TCID_{50}$) in two adsorption cycles. Following the second adsorption cycle, the cells were seeded in two 75 cm^2 flasks with 30 ml of media supplemented with FBS, antibiotics, and human IL-2 (20 Units/ml). Cell culture supernatant was collected every three days, with fresh media being added, until day 21 of culture and stored at -80 °C. A small aliquot from each collection will be used to titrate the virus using quantitative RT-PCR.

Animal experiment design

All animal procedures were approved by the UTHSCT Institutional Animal Care and Use Committee (IACUC) (Protocol #707). NOD.Cg-Prkdc^{scid} Il2rg^{tm1Wjl} Tg(CMV-IL3,CSF2,KITLG)1Eav/MloySzJ (NSG-SGM3) mice were purchased from The Jackson laboratory (Bar Harbor, ME) and bred in the Vivarium facilities at UTHSCT. Pups were weaned at 21 days after birth and, 1-3 weeks after that, they were irradiated at a dose of 100 cgy/mouse, followed by intravenous injection with 2×10^5 $CD34^+$ stem cells/mouse at 12 h post-irradiation. Humanization was monitored starting at 12 weeks after stem cell transplantation and again at 14 and 16 weeks. For this purpose, blood was drawn from the submandibular vein (100-150 µl, based

on animal weight) and PBMCs were collected through density gradient centrifugation using Ficoll Paque (Cytiva, Marlborough, MA). After erythrocyte lysis, the PBMC from each animal were stained for human (hu) and mouse (mo) hematopoietic cell surface marker ($CD45^+$), as well as lymphocytic and myeloid markers. Animals that showed a positive $huCD45^+/moCD45^+$ ratio, accompanied by differentiation of various immune cell populations, were selected for experimental infection.

Mice were randomly divided into four experimental groups: Uninfected (n=5), HIV-infected (n=8), *Mtb*-infected (n=8) and HIV/*Mtb* co-infected (n=7). *Mtb* infection was performed using aerosolized *Mtb* H37Rv through a Madison chamber, as previously described[32], using an infection dose of 100 CFU/mouse. Three additional mice were included in the Madison chamber at the time of infection and were euthanized 24 hours after infection. The lungs were collected, macerated and plated on 7H10 agar, to confirm the initial bacterial implantation[33].

One day after *Mtb* infection, the mice for the HIV alone and HIV/*Mtb* co-infection groups were subjected to intraperitoneal (IP) inoculation with 10^5 $TCID_{50}$ of HIV_{BaL}. Blood samples from all experimental groups were collected on the day of infection and at 15-, 28- and 35-days post infection (dpi). Serum samples from all the animals were separated and stored at -80 ºC until further use. PBMCs were isolated and stained for flow cytometry analysis. At 35 dpi, the animals were terminally anesthetized, using a Ketamine/Xylazine mixture, in order to perform computed tomography (CT) scan and pulmonary function (PF) tests. Afterwards, the animals were euthanized and whole blood samples were collected through cardiac punction. During necropsy, lung and spleen samples were collected and macerated through a 70 µM cell strainer (Thermo Fisher scientific) in a final volume of 2 ml of PBS. Serial ten-fold dilutions of the organ macerates

were plated in 7H10 agar, supplemented with OADC, to assess the bacterial load. The remaining volume of lung and spleen macerates were stored at -80 ºC for further analysis.

For each experimental group, lung sample from one animal was selected for histopathological analysis and, therefore, not subjected to maceration and bacterial culture. Lungs were filled with 10% formalin, before being removed from the animal, and stored in the same media after the necropsy[34, 35]. Sample processing and Hematoxylin-Eosin (HE) staining was carried out at the histopathology core of UT southwestern.

CT scan and PF testing

Mice were intraperitoneally injected with ketamine/xylazine (100 mg/kg Ketamine, 20 mg/kg Xylazine). Once the correct anesthetic plane was achieved, the mice were intubated with a sterile, 20-gauge intravenous cannula through the vocal cords into the trachea. Following intubation, anesthesia was maintained using isoflurane.

Elastance (Ers), compliance (Crs), and total lung resistance (Rrs) was assessed for each mouse through the snapshot perturbation method, as previously described[36]. Measurements were performed in triplicates for each animal, using the FlexiVent system (SCIREQ, Tempe, AZ), with a tidal volume of 30 mL/kg at a frequency of 150 breaths/min against 2–3 cm H2O positive end-expiratory pressure.

After PF testing, the mice were subjected to CT scans for the measurements of lung volume, using the Explore Locus Micro-CT Scanner (General Electric, GE Healthcare, Wauwatosa, WI). CT scans were performed during full inspiration and at a resolution of 93 μm. Lung volumes were calculated from lung renditions collected at full inspiration. Microview

176 software 2.2 (http://microview.sourceforge.net) was used to analyze lung volumes and render
177 three-dimensional images.

178 **RNA extraction and RT-qPCR**

179 Serum samples from all experimental groups were extracted using the NucleoSpin RNA
180 isolation kit (Macherey-Nagel, Allentown, PA). Following viral RNA extraction, samples were
181 evaluated using RT-qPCR to determine the viral RNA load in each animal[37]. Control standards
182 (obtained from NIH AIDS Reagent Program) with known quantities of HIV-1 genome copies were
183 used as amplification controls, as well as to stablish a standard curve that was used to determine
184 the viral RNA load, based on the cycle threshold (Ct) value.

185 **Flow cytometry analysis**

186 Flow cytometry was performed using the PBMCs from all experimental animals at the
187 specified sampling timepoints. In all cases, the PBMCs isolated from each animal were divided
188 into two wells of a 96-well U-shaped bottom plate (Corning Inc., Corning, NY), used for staining
189 with two separate flow cytometry panels. Cells were washed and inoculated with Fc block
190 (Biolegend, San Diego, CA) at 4 ºC for 20 minutes, followed by another wash. Afterwards, cells
191 were incubated with fluorescence-conjugated monoclonal antibodies. For the first flow cytometry
192 panel, cells were incubated with antibodies against the following human surface markers: Alexa
193 Fluor™ 405-CD45, FITC-CD3, APC-CD4, PE-CD8, PerCP-CD56, Alexa Fluor™ 510-CD19
194 (Biolegend, San Diego, CA). For the second flow cytometry panel, the antibodies against human
195 cell surface markers were as follows: Alexa Fluor™ 405-CD45, Alexa Fluor™ 510-CD86, APC-
196 CD11b, PE-CD11c, PerCP-HLA-DR, Alexa Fluor™ 700-CD14 (Biolegend, San Diego, CA).
197 Additionally, for the second panel, the cells were also incubated with an FITC-labelled antibody

198 against moCD45. After staining, the cells were washed and fixed for 1 hour, followed by another
199 wash. Flow cytometry was performed using the Attune NxT flow cytometer (Invitrogen, Waltham,
200 MA), including the corresponding isotype controls for each antibody. Analysis was carried out
201 with the FlowJo software v10.6.1 (BD life sciences), using the isotype controls as guidelines for
202 gating.

203 **Immunofluorescence staining**

204 Paraffin-embedded lung sections were used for immunofluorescent staining against human
205 immune cell subsets[38]. Samples were deparaffined by submerging the slides in Xylene (Fisher
206 bioreagents), followed by sequentially lower concentrations of ethanol. Afterwards, antigen
207 retrieval and blocking of non-specific binding were performed, using 10mM sodium citrate buffer
208 and PBS with 0.4% triton and 5% FBS, respectively. Primary antibody incubation was carried out
209 overnight at 4 °C with human-CD68 monoclonal antibody (cat. No. 14-0688-82, Invitrogen) and
210 CD19 Rabbit polyclonal antibody (cat. No. 27949-1-AP, Proteintech, Rosemont, USA), diluted in
211 PBS + 0.4% triton + 1% FBS at the recommended dilutions. The following day, samples were
212 incubated for 2 hours at room temperature with goat anti-mouse IgG1-Alexa Fluor™ 568 (cat. No.
213 A21124, Invitrogen) and goat anti-rabbit IgG-Alexa Fluor™ 488 (cat. No. A11008, Invitrogen), at
214 the recommended dilutions. The slides were mounted using DAPI-supplemented mounting
215 medium (Abcam, Cambridge, UK) and images were captured with a LionheartLX automated
216 microscope (Biotek, Winoovski, VT). Images were processed with the GEN5 software version
217 3.09 (Biotek) and the ImageJ software (NIH).

218 **Multiplex assay for cytokine profiling**

The cytokine profile in lung and spleen tissue macerate, as well as serum samples at 35 dpi, from all experimental groups were evaluated in duplicates using the Bio-Plex Pro™ Human Cytokine panel (Bio-Rad, Hercules, CA), according to the manufacturer's instructions. Briefly, 50 µL of filtered tissue homogenate, or 1:4 diluted serum, were dispensed in a 96-well plate containing magnetic beads conjugated with antibodies for the detection of 27 different cytokines. Following incubation with detection antibodies and streptavidin-PE, the samples were analyzed in the Bio-Plex MAGPIX multiplex reader (Bio-Rad Laboratories Inc., CA). A regression curve, based on the values obtained from a set of standard dilutions, was used to convert the fluorescence values reported by the machine into cytokine concentrations (expressed as pg/mL).

The 27 cytokines and chemokines reported by the Bio-Plex Pro™ Human Cytokine panel were: Basic FGF, Eotaxin, G-CSF, GM-CSF, IFN-γ, IL-1β, IL-1Ra, IL-2, IL-4, IL-5, IL-6, IL-7, IL-8, IL-9, IL-10, IL-12, IL-13, IL-15, IL-17, IP-10, MCP-1, MIP-1α, MIP-1β, PDGF-BB, RANTES, TNF-α and VEGF.

Mouse blood sample handling for metabolomic analysis

Whole blood sample was collected from mice in all the experimental groups at the end of the study and plasma was separated through centrifugation. The samples were processed for collection of the metabolite pellet as follows: 50 µl of plasma were mixed with 950 µl of 80% ice-cold methanol, followed by centrifugation at >20.000 G for 15 minutes in a refrigerated centrifuge. Afterwards, the supernatant was transferred to a new tube and vacuum dried, using no heat. The metabolite pellet was analyzed at the metabolomic core facility at the Children's Medical Center Research Institute at University of Texas Southwestern Medical Center (Dallas, TX, USA) using liquid chromatography–mass spectrometry (LC-MS), as previously described[39].

Metabolome data analysis

Statistical analysis of metabolome profiles was performed in R environment (R version 4.1.0). Raw abundance values of metabolites were used as input for statistical analysis. The raw data was log2 transformed and normalized across the samples using 'limma' package[40] by cyclically applying fast linear loess normalization with a 0.3 span of loess smoothing window and 10 iterations wherein each sample was normalized to pseudo-reference sample which was computed by averaging all samples. Principal components analysis was performed using 'PCAtools' package. Orthogonal partial least squares discriminant analysis (OPLS-DA) was performed and variable importance on projection (VIP) score were computed using 'ropls' package. VIP score of >1 is considered for feature selection. Hierarchical clustering was performed on normalized data after univariate scaling. Hierarchical clustering was performed using correlation to calculate clustering distance with averaging method for clustering. Differentially abundant metabolites (DAMs) were identified using student t test. The correlation between metabolite abundances and *Mtb* or HIV loads were analyzed using Pearson correlation method. For all hypothesis testing analyses, statistical significance was set 5% (p value = 0.05) to reject null hypothesis.

Statistical analysis

Statistical differences between groups were assessed using the Prism software version 8.3.0. for Windows (GraphPad Software, San Diego, California USA, www.graphpad.com). Unpaired, non-parametric, t-tests were employed for different comparisons between groups.

RESULTS

Human CD34+ HSCs-engrafted NSG-SGM3 mice can differentiate a full array of human immune cell phenotypes.

After 16 weeks of humanization, PBMCs from the hCD34^{+} HSCs-transplanted mice were evaluated by flow cytometry for human lymphoid and myeloid cell surface markers. The NSG-SGM3 mice allow stem cells to develop into human lymphoid lineages, such as T cells (CD3^{+}, between 10-90%, including both CD4+ and CD8+ T cells) and B cells (CD19^{+}, between 7-60%) (**Fig. 1**). Additionally, differentiation of human myeloid subsets (CD14^{+}) was also observed, ranging between 1 and 25%. Within the myeloid lineage, we also detected CD11b+ macrophages (**Fig. 1,** Gating strategy is shown in **Supplementary Fig. 1**).

Humanized NSG-SGM3 mice are susceptible to both HIV-1 and *Mtb* infections.

After HIV/*Mtb* infections, HIV viral RNA was detected in serum samples from the infected mice starting at 15 dpi, with most animals in the HIV single-infection group being positive at this time, while only two out of the seven mice in the HIV/*Mtb* co-infection group showed viral RNA (**Fig. 2a**). The viral RNA load detected in the positive animals at 15 dpi was between 2×10^5 and 2.2×10^6 copies/ml. However, all the HIV-infected animals were positive in subsequent samplings at 28 and 35 dpi. The HIV RNA load was between 3.7×10^4 and 6.8×10^5 copies/ml for animals with single HIV infection and between 4.1×10^4 and 7.7×10^5 copies/ml for the HIV/*Mtb* co-infected mice. No significant differences were detected in the viral RNA load between the two HIV-infected groups at these timepoints.

The *Mtb* bacterial load was assessed in lung and spleen samples after euthanasia in the *Mtb* single infection group and the HIV/*Mtb* coinfected mice (**Fig. 2b**). In both groups, a higher

bacterial load was found in lungs than in spleens. Moreover, the mean CFU count in the lungs and spleens from *Mtb* single infection group (7.3×10^6 and 1.4×10^6, respectively) was higher than the animals co-infected with HIV (5.8×10^6 for lung and 9.2×10^5 for spleen), even though their differences are not significant (**Fig. 2b**).

Immune phenotype changes in humanized mice after infection.

We also monitored the human immune cell population changes over time after HIV/*Mtb* infections. Starting from 15 dpi, $huCD45^+/moCD45^+$ ratio was significantly decreased ($p<0.05$) in the two HIV-infected groups (HIV single infection and HIV/*Mtb* co-infection), and the $huCD45^+/moCD45^+$ ratio decrease was sustained until the late stage of the experiment. Conversely, the *Mtb* single infection group showed similar or even increased $huCD45^+/moCD45^+$ ratio after infection (**Fig. 3a**).

We observed significant $CD4^+$ T cell depletion in the HIV-infected groups (HIV single infection and HIV/*Mtb* co-infection). We used $CD4^+/CD8^+$ ratio as an indicator for $CD4^+$ T cell depletion, and we found a ~10-fold $CD4^+/CD8^+$ reduction ($p<0.05$) in the HIV/*Mtb* co-infected mice as early as 15 dpi, and this trend remained until the end of the experiment. In the single infection group, we also found a lower mean $CD4^+/CD8^+$ ratio since 15 dpi, while the subsequent samplings at 28 and 35 dpi showed significant decreases on $CD4^+/CD8^+$ ratio values. In contrast, there was no significant difference detected over time in the Mtb alone infection group (**Fig. 3b**).

Alterations in cytokines and chemokines production in humanized mice after infection

In serum sample, significant increases in G-CSF, MCP-1 and MIP-1α was detected in the *Mtb* single infection group, in comparison with both HIV-infected groups (**Fig. 4a**). Additionally, the serum concentration of IL-2 and IL-8 were also significantly increased in the *Mtb* single

infection group, compared to the HIV/*Mtb* co-infection. The HIV/*Mtb* co-infected mice analyzed showed higher IP-10 than both the HIV and *Mtb* single infection mice (**Fig. 4a**).

Lung macerate supernatants showed an increase in the concentration of IL-6, RANTES and TNF-α in the HIV single infection group compared to the uninfected control animals, as well as the Mtb single infection group (**Fig. 4b**). Additionally, IL-2 concentrations were also higher in the HIV-infected animals than in the uninfected mice. Moreover, HIV single infection also induced statistically higher levels of Eotaxin, MIP-1α and MIP-1β than single *Mtb* infection. Statistical analysis also revealed a decrease in MCP-1 and PDGF concentration in lung samples from *Mtb* infected mice, compared to the remaining three experimental groups (**Fig. 4b**).

In the case of spleen samples, macerates from the *Mtb* single-infection group were found to have significantly higher concentrations of IL-1β, G-CSF and MIP-1β than the HIV single-infection group (**Fig. 4c**). Similarly, the levels of IL-8 and MIP-1α were higher in the *Mtb* group than in both HIV-infected groups. In contrast, both the HIV and *Mtb* single infection groups showed lower concentrations of GM-CSF than the HIV/*Mtb* co-infected animals, while this group also had statistically higher amounts of IFN-γ than the *Mtb* group. All the infected groups showed a decrease in IL-1Rα and IL-13, compared to the uninfected control animals (**Fig. 4c**).

***Mtb* infection induced pathological changes in the lungs of humanized mice.**

We stained the lung section with H&E staining, and we observed diffuse immune cell infiltration in lung sample from *Mtb*-infected mice. In some cases, immune cell infiltration was observed around a necrotic nucleus, in structures similar to TB granulomas. No such cellular aggregates were detected in either the uninfected or the HIV single infection groups (**Fig. 5a**). We stained lung sections from *Mtb*-infected humanized mice by immunofluorescent staining, and the

result showed that the cell populations surrounding the necrotic area mostly corresponded with macrophages ($CD68^+$), though other immune cell types, such as $CD19^+$ B cells, were also found. However, no granuloma structure was observed in the lung section of the uninfected mice, even though a low proportion of cells expressing the human $CD68^+$ and $CD19^+$ surface markers was observed in the lung sections from uninfected mice (**Fig. 5b**).

The CT scan showed an increase in high density areas in the *Mtb*-infected animals, regardless of their HIV-infection status, indicating the occurrence of inflammation and other pathological changes in the lungs (**Fig. 5c**). However, no significant differences were detected in the pulmonary function tests between the experimental groups (**Fig. 5d**).

Different plasma metabolome landscapes in healthy mice, HIV infection, *Mtb* infection and co-infection.

Plasma metabolome profiling was performed for a total of 10 samples including no infection (n=3), *Mtb* infection (n=3), HIV infection (n=2), and HIV/*Mtb* co-infection (n=2). Abundances of 175 metabolites were estimated. To enable comparison of metabolite abundances between different samples, data was normalized across the samples. To investigate differences in plasma metabolome landscape among the four categories of infection, principal components analysis (PCA) was performed. PCA is an unsupervised learning method suitable for dimensionality reduction of high dimensional metabolome data. Interestingly, the plasma metabolome profiles are stratified according to infection status in PCA (**Fig. 6a**). Mice with no infection appeared distinct from all infected mice. While the mice with infections were clustered separately from healthy mice, there was a clear distinction among HIV infection alone, *Mtb* infection alone, and HIV/*Mtb* co-infection. This suggests that the global plasma metabolome is distinctly altered based on infection status and type. Interestingly, the samples from HIV/*Mtb* co-

352 infected mice clustered in between HIV infection alone and *Mtb* infection alone suggesting they
353 show metabolic changes common for individual infections.

354 To identify metabolites varying across the four categories, we performed OPLS-DA
355 followed by computation of VIP scores on all 175 metabolites. OPLS-DA is a supervised analysis
356 which helps in identifying variables that discriminate different categories of samples based on VIP
357 score. There were 75 metabolites with a VIP score >1 (**Supplementary Table 1**). The abundances
358 of these metabolites across all four categories were shown with hierarchical clustering (an
359 unsupervised algorithm) in **Fig. 6b**. As expected, in concordance with PCA, dendrogram of
360 hierarchical clustering showed that infection and no infection categories are distinct, while co-
361 infection stratified between the two individual infections (**Fig. 6b**).

362 To identify metabolites that are differentially abundant in HIV infection, we compared
363 healthy mice (n=3) to HIV infection mice (n=4; HIV infection alone and HIV/*Mtb* co-infection).
364 We identified 8 DAMs in HIV infection with a p value <0.05 (**Fig. 6c** and **Table 1**). Similarly, we
365 compared healthy mice (n=3) to *Mtb* infection mice (n=5; *Mtb* infection alone and HIV/*Mtb* co-
366 infection) to identify metabolites differentially abundant in *Mtb* infection which yielded 13 DAMs
367 (**Fig. 6d** and **Table 2**). Interestingly, three fatty acids, namely dodecanoic acid, palmitic acid and
368 myristic acid exhibited reduced abundance in HIV infected mice as well as *Mtb* infection mice
369 (**Table 1** and **2**).

370 **Metabolite abundances correlated with HIV and *Mtb* loads.**

371 To identify metabolites correlating with HIV or *Mtb* load with metabolites, we used
372 Pearson correlation analysis. HIV infection load (as detected by RNA copies/ml plasma) positively

correlated with diethanolamine (r=0.99), and negatively correlated with glucose 6-phosphate/mannose 6-phosphate (r=-0.95) and imidazole acetic acid (r=-0.92) (**Fig. 7A**).

Next, we observed that *Mtb*-infected mice did not show a strong correlation (r=0.68) between pathogen load (as measured by colony forming units per organ) in the lungs and spleens (**Supplementary Fig. 2**) underscoring the heterogeneity of *Mtb* distribution in these organs of the humanized mice. This is consistent with an earlier report[41] showing that increase of *Mtb* load in the lungs and spleens follow different trajectories over the course of infection. Therefore, we analyzed the correlation between metabolites abundances and *Mtb* load in spleens and lungs separately.

Interestingly, none of the metabolites correlated with the HIV load (shown in **Fig. 6c**) exhibited correlation either positively or negatively with *Mtb* load in lung or spleen. However, PC(16:0/18:1(11Z)) and lysoPC(16:0/0:0) positively correlated with *Mtb* load in lung as well as spleen (**Fig. 7b**). In addition, 3-hydroxyheptanoic acid exhibited a strong negative correlation with *Mtb* load in lung (**Fig. 7b**). Similarly, LysoPC(18:1/0:0) showed strong positive correlation, and myristic acid, PC(20:3(5Z,8Z,11Z)/20:3(5Z,8Z,11Z)) and PC(18:2(9Z,12Z)/16:0) showed strong negative correlation with *Mtb* load of the spleens (**Fig. 7c**).

DISCUSSION

The development of animal models is a major requirement for developing drugs and vaccines for infectious diseases[42-44]. The lack of an ideal animal model can therefore delay the development of intervention strategies that can improve the outcome of disease in humans. The study of the interactions taking place during HIV/*Mtb* co-infection is particularly challenging due

to a variety of factors, related to the nature of these pathogens, and the animal models. In this study, we demonstrated a reliable and reproducible small animal model for HIV/*Mtb* co-infection research using humanized NSG-SGM3 mice. We show that our model can recapitulate many aspects of HIV/*Mtb* co-infection in clinical settings, which will be helpful for characterizing the HIV/*Mtb*-induced immunopathogenesis, and to test therapeutics and vaccines.

A primary concern with using the mouse models for HIV/*Mtb* co-infection studies relates to the viral host range, which is naturally limited to humans and some NHPs[45, 46]. This poses restrictions on experimentation using NHPs, which require specialized infrastructure and personal training that is not widely available [8]. However, this limitation has been circumvented to some extent by the use of immunocompromised mice strains that can engraft human stem cells and differentiate them into a variety of human immune cells, allowing for both HIV and *Mtb* infection and viral replication[14, 15, 18, 19, 47]. We show that the NSG-SGM3 mice allow stem cells to differentiate into a range of immune cells becoming susceptible to HIV infection and viral replication. This is due to the differentiation of human lymphoid lineage cell subsets, in particular generation of $CD4^+$ T cells, which are the major target for HIV infection and replication. Moreover, the abundant differentiation of both lymphoid and myeloid lineage subsets allows for the assessment of immunological markers of disease relevance during HIV infection, and to measure vaccination-induced immune responses. A decreased $CD4^+/CD8^+$ ratio was observed in the humanized mice following HIV-1 infection, suggesting that our model reproduced similar immunological alterations observed during the natural infection of humans[48, 49].

A comparative advantage that the NSG-SGM3 mice used in the present study over the previous generation of humanized mouse models is the transgenic expression of three human cytokine genes that enhance the differentiation and maturation of myeloid cell lineages and

418 regulatory T cells[14]. This is particularly important, considering that these immune cells play
419 important roles in controlling both HIV and *Mtb* growth and also serve as the target cells for these
420 pathogens[50-53, 54, 55]. Moreover, the presence of granulomas, which are the hallmark of *Mtb*
421 pathology, in the *Mtb*-infected humanized NSG-SGM3 mice is noteworthy, given that these
422 structures are composed of multiple human immune cell populations from different lineages, that
423 has not been seen in the C57BL/6 or BALB/c mice[56]. In addition, the previously reported
424 humanized NSG-BLT mice required specialized surgical procedures in adult mice[19], or the
425 handling of newborns[14]. The humanization of NSG-SGM3 mice only requires a single intravenous
426 injection of stem cells, which makes humanization much simpler to produce a viable small animal
427 model for HIV/*Mtb* research.

428 We further note the differential expression of multiple human cytokines by the NSG-SGM3
429 humanized mice after HIV and *Mtb* single-infection or co-infection, which indicates that the
430 reconstituted human immune cell subsets in these animals are functional and responsive during
431 the infectious process. It should be noted that many of the cytokines that showed increased levels
432 of expression in tissues after infection, were colony stimulating factors (G-CSF and GM-CSF) or
433 chemoatractants (MCP-1, MIP-1α, MIP-1β), which have been implicated in human immune
434 response against HIV and *Mtb*[57-62]. This indicates that immune cell recruitment and differentiation
435 diverge according to the immune response induced by these pathogens in our model. Moreover,
436 each tissue exhibited a different cytokine production profile. This could be due to the difference in
437 cell types present in the tissues, as well as the viral/bacterial load and its effect on the immune
438 response. In this regard, we noted that cytokine production did not increase in the lungs of the
439 *Mtb* infection group, despite having a high bacterial load confirmed by culture. This is interesting
440 and may suggest that *Mtb* suppresses lung immune responses to enhance its growth[52, 63-65].

441 Nevertheless, cytokine expression in spleens was increased in the *Mtb*-infected mice, indicating
442 immune activation in this organ. Similarly, the results of the Pearson correlation in plasma
443 metabolites from the HIV-infected mice likely reflect the immune modulation by the pathogen,
444 considering the positive correlation of viral load with an immunostimulatory xenobiotic
445 (diethanolamine)[66], while an inverse correlation was found with a subproduct of histamine
446 metabolism (Imidazoleacetic acid)[67]. Although additional investigations are required, these results
447 suggests concurrent activation of immune response, and suppression of the inflammation
448 pathway; this coincides with earlier reports which show that histamine release is inversely
449 correlated to the number of HIV-infected CD4+ T cells in humans[68]. The differences in cytokine
450 and metabolite production may also reflect different stages of disease, and further studies are
451 needed to validate these hypotheses.

452 The metabolome data also provided insight into the disruptions of the immunometabolism
453 after HIV/*Mtb* infections in the humanized mice. It is noteworthy that the majority of the DAMs
454 detected in the present study for both HIV and *Mtb* infection are fatty acids or metabolites involved
455 in their metabolism. In accordance with previous reports, triglycerides were found to be increased
456 in the plasma of HIV-infected mice, regardless of *Mtb* infection status[69]. Thus,
457 Lysophosphatidylcholines (LysoPC), such as LysoPC (16:0/0:0), have been found to be increased
458 in HIV-infected individuals[70]. Paradoxically, the concentration of palmitic acid (16:0), the fatty
459 acid attached to the C-1 position of LysoPC (16:0/0:0), was found to be decreased in HIV-infected
460 mice compared to the uninfected controls, suggesting a disruption in fatty acid metabolism.
461 Moreover, dodecanoic (12:0), myristic (14:0) and arachidic (20:0) acids were also decreased in the
462 HIV-infected mice, in line with a previous study that reported a reduction in free fatty acid
463 concentration in serum from people living with HIV, which increased after antiretroviral

464 treatment[71]. On the other hand, Pearson correlation showed an inverse relation between HIV load
465 and imidazoleacetic acid, an imidazole receptor stimulator. Given the anti-HIV potential of the
466 imidazole derivatives[72, 73], the higher concentration of imidazoleacetic acid may facilitate the
467 imidazole receptor binding, thus activating the imidazole-mediated anti-HIV capacity, and a lower
468 HIV load. In addition, glucose metabolic pathways in regulating HIV infection in CD4+ T cells
469 have been extensively reported[74, 75]. HIV infection increases glucose uptake in CD4+ T cells, and
470 consequently, a higher glucose uptake by the CD4+ T cells will result in a lower concentration of
471 glucose left in the serum; therefore, it was not surprising to see a negative correlation between HIV
472 load and the metabolite glucose/mannose 6-phosphate in the serum (**Fig 7a)**.

473 In the case of *Mtb* infection, multiple DAMs related to TB pathogenesis were found in the
474 plasma of infected mice (Table 2). Platelet-activating factor, increased in the *Mtb*-infected mice,
475 has been previously shown to be an important part of TB immunopathology, and present in TB
476 granulomas of humans and participating in the activation of other immune cell types during
477 infection[76]. Meanwhile, N^6-(Δ^2-isopentenyl) adenine, a cytokinin previously thought to be
478 produced only in plants, has been recently proven to be produced by *Mtb* (thus significantly
479 increased in *Mtb*-infected mice), likely having a role in the protection of *Mtb* against nitric oxide[77].
480 Interestingly, three fatty acids (Dodecanoic acid, Myristic acid, and Palmitic acid) that were
481 decreased in the HIV-infected mice were also decreased in plasma from *Mtb*-infected humanized
482 mice, in addition to gluconic acid (6:0). The fatty acids alterations reflected the changes of
483 mitochondrial function and β-oxidation, and this also is also evidenced by the reduction of L-
484 carnitine, a metabolite necessary for the uptake of large chain fatty acids by the mitochondria[78].
485 We recall here that lipid-related metabolites have been reported to be decreased in humans co-
486 infected with HIV and *Mtb*[79]. It has been reported that *Mtb* can alter lipid metabolism in

487 macrophages, reducing the rate of ATP production, while at the same time, increasing their
488 dependence on exogenous rather than endogenous fatty acids[80]. We therefore propose that the
489 decrease of free fatty acids in the plasma of *Mtb*-infected animals might be related to sequestering
490 of the pathogen in the macrophages[81].

491 Collectively, our study shows that the NSG-SGM3 humanized mice can efficiently engraft
492 human CD34+ stem cells which differentiate into a full lineage of functional immune cells. These
493 mice are susceptible to both HIV-1 and *Mtb* infections, and the HIV/*Mtb* infections cause similar
494 immunological, pathological, and metabolic changes in these mice as in humans. Therefore, the
495 humanized NSG-SGM3 mice recapitulate the human-like immune responses to HIV/*Mtb*
496 infections.

497

498 **Data availability**

499 All data supporting the findings of this study are available in the manuscript. If there are any
500 special requests or questions for the data, please contact the corresponding author (G.Y.).

501

502 **Acknowledgments**

503 We thank Dr. Amy Tvinnereim for helping perform the following experiments: Irradiated the mice
504 and performed *Mtb* infection of the humanized mice.

505

506 **Funding:**

507 This work was partially supported by the NIH Common funds and the National Institute of Allergy
508 and Infectious Diseases grant UG3AI150550, and the National Heart, Lung, and Blood Institute
509 grant R01HL125016 to G.Y., and National Institute of Allergy and Infectious Diseases grant 1RO1
510 AI161015 to C.J.

511

512

513

Contributions

Guohua Yi: Conceived and guided the study, designed experiments, analyzed data, edited figures, and wrote and finalized the manuscript.

José Alejandro Bohórquez: Designed and performed the experiments, analyzed data, made the figures, and wrote the manuscript.

Sitaramaraju Adduri: Performed the experiments, analyzed data, made the figures, and wrote the manuscript.

Danish Ansari: Performed the experiments.

Sahana John: Performed the experiments.

Jon Florence: Performed the experiments and analyzed data.

Omoyeni Adejare: Performed the experiments.

Gaurav Singh: Performed the experiments.

Nagarjun Konduru: Edited the manuscript.

Chinnaswamy Jagannath: Provided guidance on experimental design and edited the manuscript.

Competing interests

All the authors declare no competing interests.

FIGURE LEGENDS

Figure 1. Human CD34$^+$ hematopointci stem cells (HSC) engraftment and differentiation of human immune cells in the **NSG-SGM3 mice. (A** and **B)**: The differential expression of humanCD45 (huCD45) and mouseCD45 (moCD45) expressing cells in mice after 14 weeks of humanization. Percentages of human and mouse CD45$^+$ cells are shown as histogram in A (n=27), and the representative flow cytometry dot plot of the comparative expression of human cell surface markers between the humanized NSG-SGM3 mice and human PBMCs are shown in B. **(C)**

Percentages of human immune cell populations (n=27). **(D)** representative flow cytometry dot plot of T lymphocytes, B cells and myeloid cells.

Figure 2. Establishment of HIV-1 and *Mycobacterium tuberculosis (Mtb)* infections in humanized mice. (A) HIV-1 RNA load, expressed as genome copies/mL, was assessed in serum samples from all experimental groups at three different timepoints of the study **(B)** *Mtb* bacterial load in lungs and spleens, expressed as CFU/organ, was evaluated in all experimental groups at the end of the study.

Figure 3. Immune cell phenotype changes after HIV-1 and *Mtb* infections. $HuCD45^+/moCD45^+$ ratio **(A)** and $CD4^+/CD8^+$ ratio **(B)** were calculated for each infected animal at different timepoints after infection. Asterisk indicates statistically significant differences ($p<0.05$, what test)

Figure 4. Cytokine profiles (Heatmap) in serum, lung and spleen samples. The Bio-Plex Pro™ Human Cytokine panel was used in the multiplex assay to evaluate the concentrations of 27 different human cytokines, which are expressed as pg/ml. **(A)** Cytokine profile of lung samples. **(B)** Cytokine profile of spleen samples. **(C)** Cytokine profile of serum samples. the letters under the columns show differences as follows: **A**: Difference between uninfected and HIV-infected, **B**: Difference between uninfected and *Mtb*-infected, **C**: difference between uninfected and HIV/*Mtb*-coinfected, **D**: Difference between HIV-infected and *Mtb*-infected, **E**: difference between HIV-infected and HIV/*Mtb*-coinfected, and **F**: Difference between *Mtb*-infected and HIV/*Mtb*-

562 coinfected. ($p<0.05$; unpaired T test). Note: The black color on the right of heatmap shows the far
563 high value that are out-of-range levels.

564

565 **Figure 5. Histopathological, radiological and functional changes in the lungs of NSG-SGM3**
566 **mice after HIV/*Mtb* infection and coinfection. (A)** Lung sections were obtained from formalin-
567 fixed tissues of animals in all experimental groups (one animal for each group) and subjected to
568 hematoxylin-eosin staining, two different amplifications are shown. **(B)** Immunofluorescence
569 staining of surface markers for human macrophages (CD68-Alexafluor 568, in orange) and B-cells
570 (CD19-Alexa 488, in green) in lung sections from uninfected and *Mtb*-infected mice. DAPI-
571 supplemented mounting buffer (in blue) was used for nuclei staining. **(C)** Representative 3D
572 renditions of CT scan and lung volume pictures obtained from animals in all experimental groups.
573 **(D)** Pulmonary function test parameters: Resistance (Rrs), compliance (Crs) and elastance (Ers),
574 were collected from animals in all experimental groups at the end of the trial (Uninfected: n=5;
575 HIV-infected: n=8; *Mtb*-infected: n=8; HIV/*Mtb*-co-infected: n=7).

576

577 **Figure 6. Metabolomics analysis of the plasma from healthy and HIV and/or *Mtb*-infected**
578 **humanized mice. (A)** Principal components analysis of plasma metabolome profiles of mice from
579 no infection (n=3), *Mtb* infection (n=3), HIV infection (n=2), and dual infection (n=2) categories.
580 Two principal components were selected to plot a two-dimensional graph to depict variation across
581 the sample categories. Variance explained by each of the two components was given in parenthesis.
582 **(B)** Heatmap showing abundances of 75 metabolites with a VIP score > 1 computed in OPLS-DA
583 on plasma metabolome profiles of mice from no infection (n=3), *Mtb* infection (n=3), HIV

infection (n=2), and dual infection (n=2) categories. Normalized data was scaled using univariate scaling. Hierarchical clustering was performed using correlation to calculate clustering distance with averaging method for clustering. **(C** and **D)** Heatmap showing differentially abundant metabolites in (**C**) HIV infection and (**D**) *Mtb* infection compared with healthy mice. Normalized data was scaled using univariate scaling. Hierarchical clustering was performed using correlation to calculate clustering distance with averaging method for clustering.

Figure 7. Scatter plots show Pearson correlation between metabolites and HIV/*Mtb* load in mice. (A) Pearson correlation between metabolites and serum HIV load (viral copies/ml). **(B)** Pearson correlation between metabolites and *Mtb* load in lungs (CFU/lung). **(C)** Pearson correlation between metabolites and *Mtb* load in spleens (CFU/spleen). Y axis shows normalized metabolites abundance values. Dotted curves show 95% confidence interval of model fit. r denotes Pearson correlation coefficient.

602 **Figures:**

603 **Figure 1.**

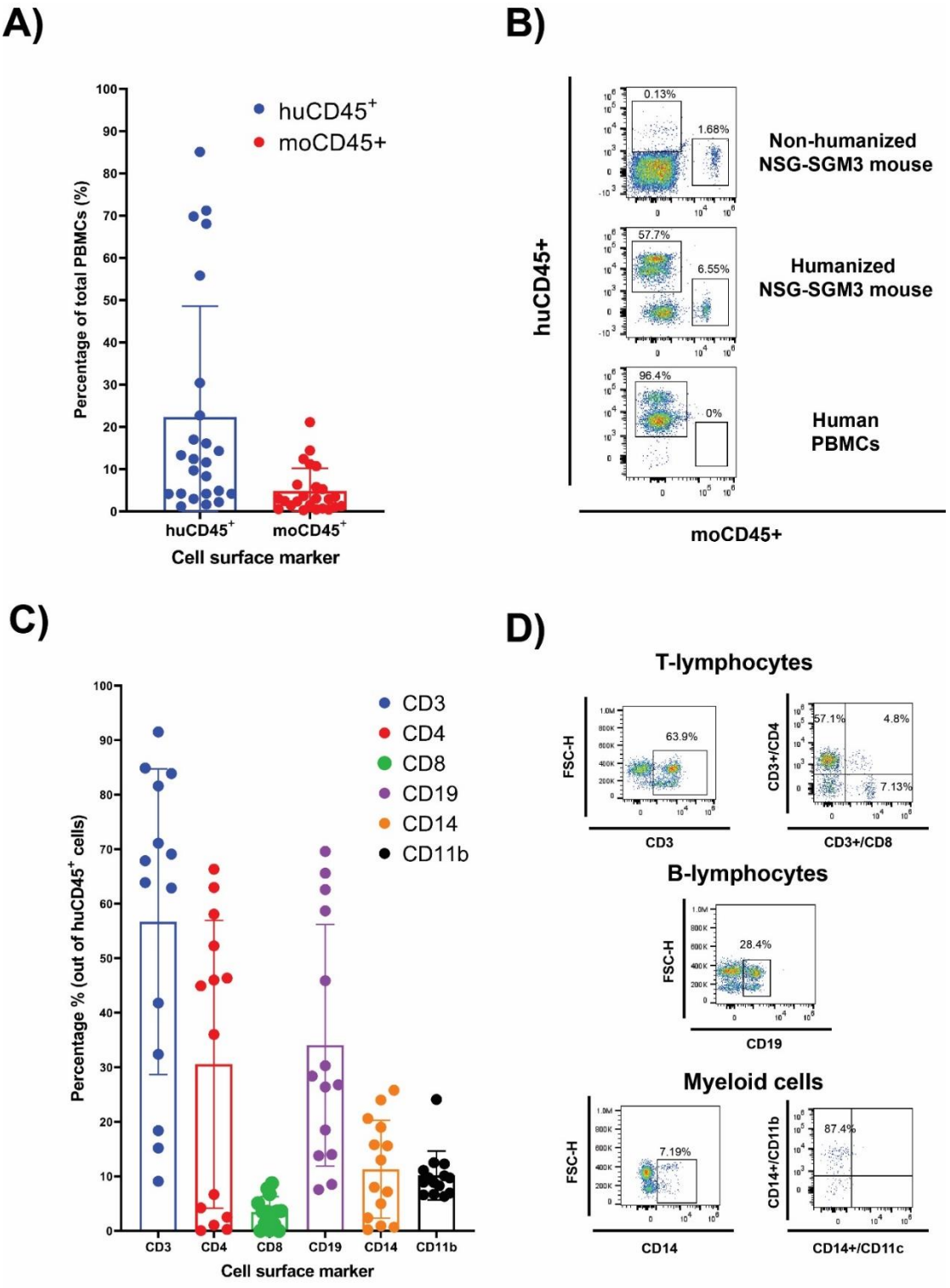

604

605 **Figure 2.**

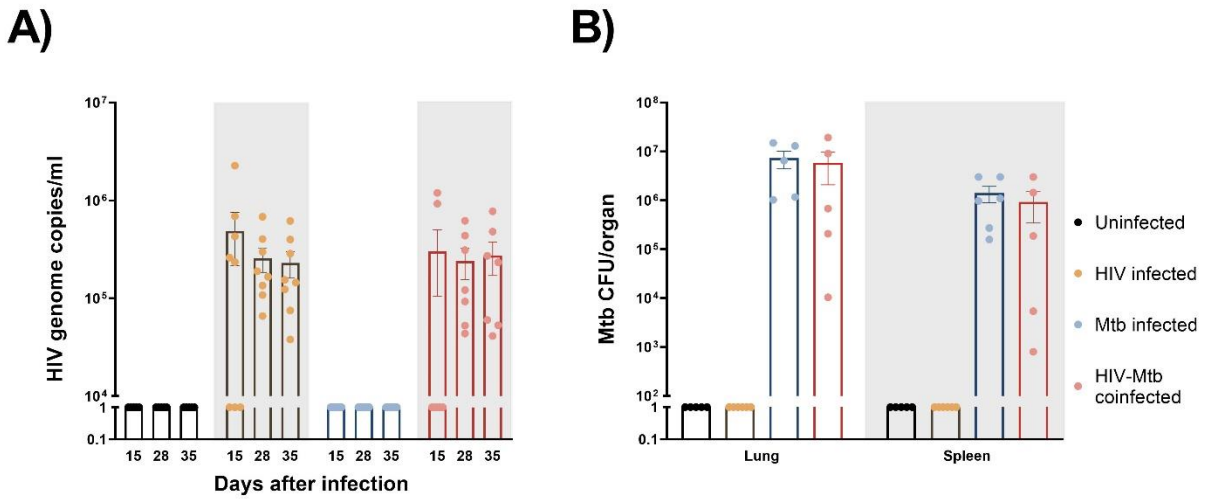

606

607

608 **Figure 3.**

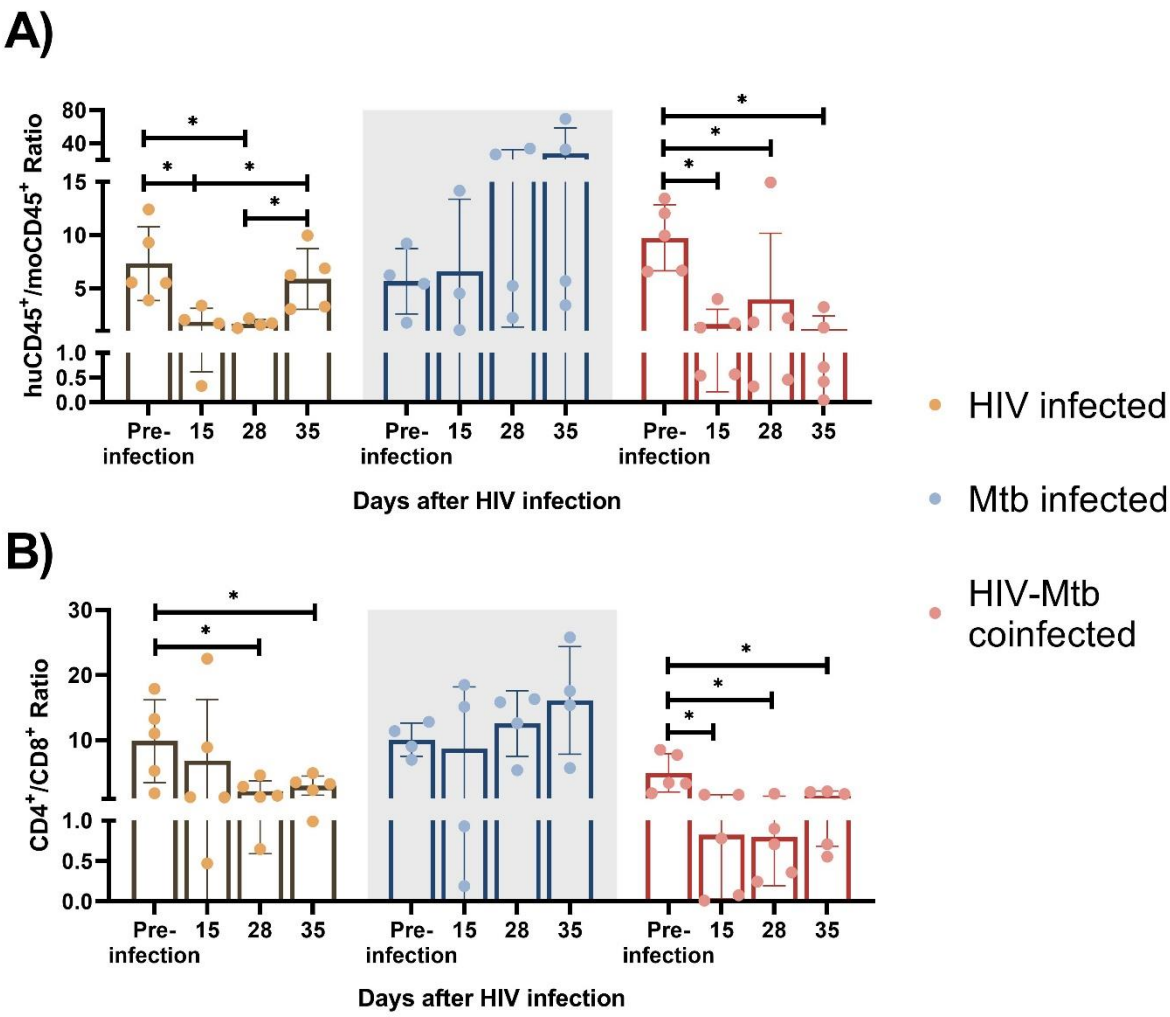

609

610

Figure 4.

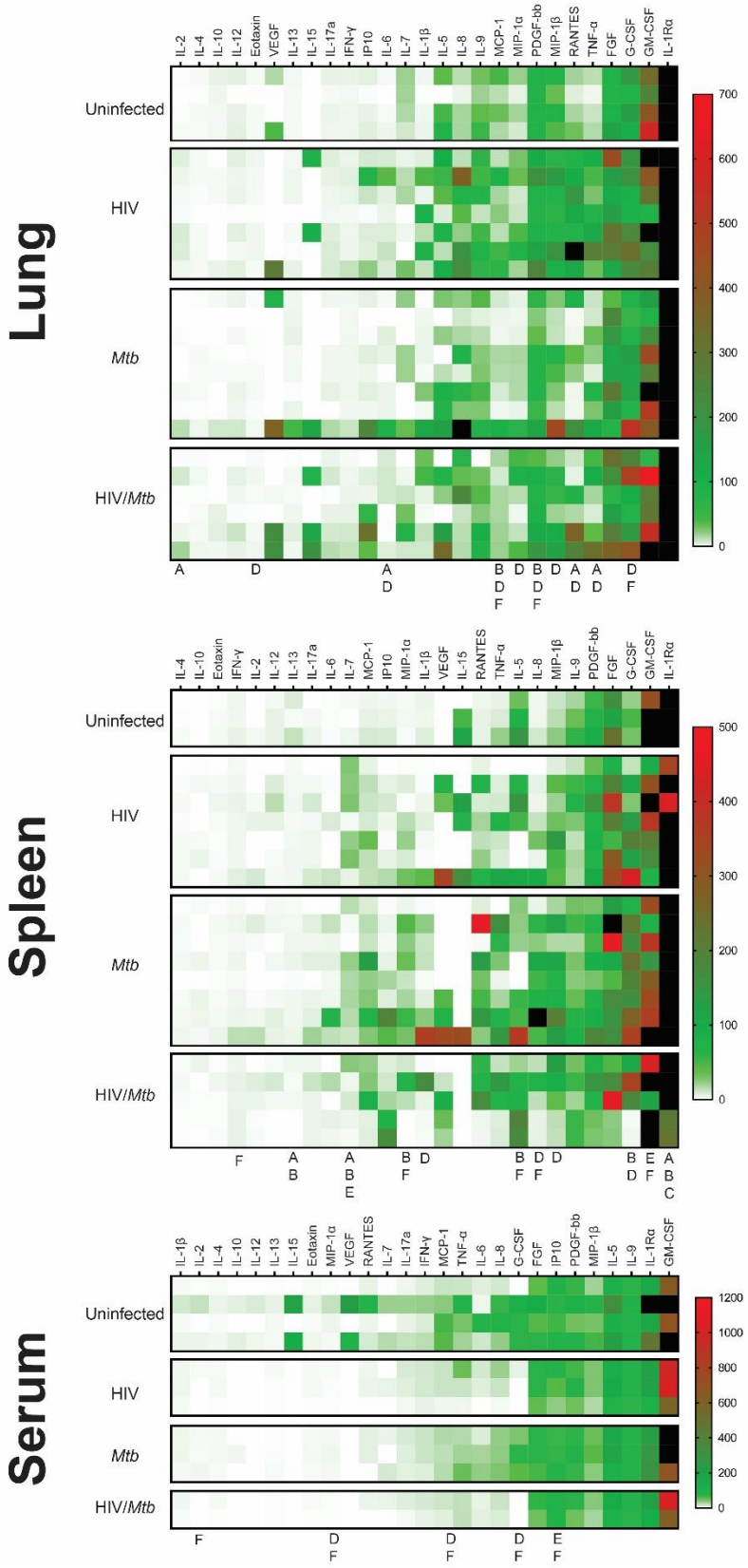

613 **Figure 5.**

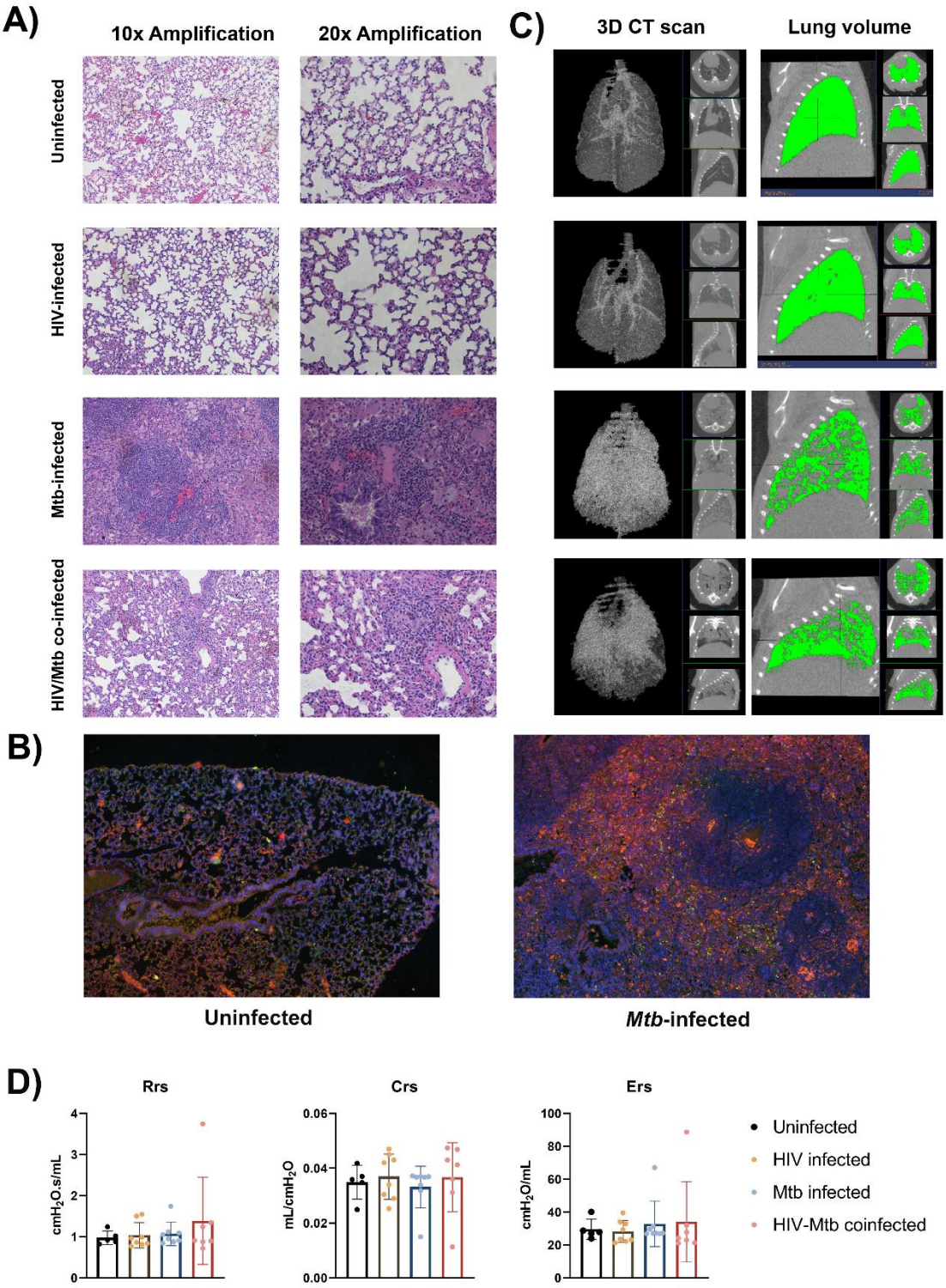

614

615

616 **Figure 6.**

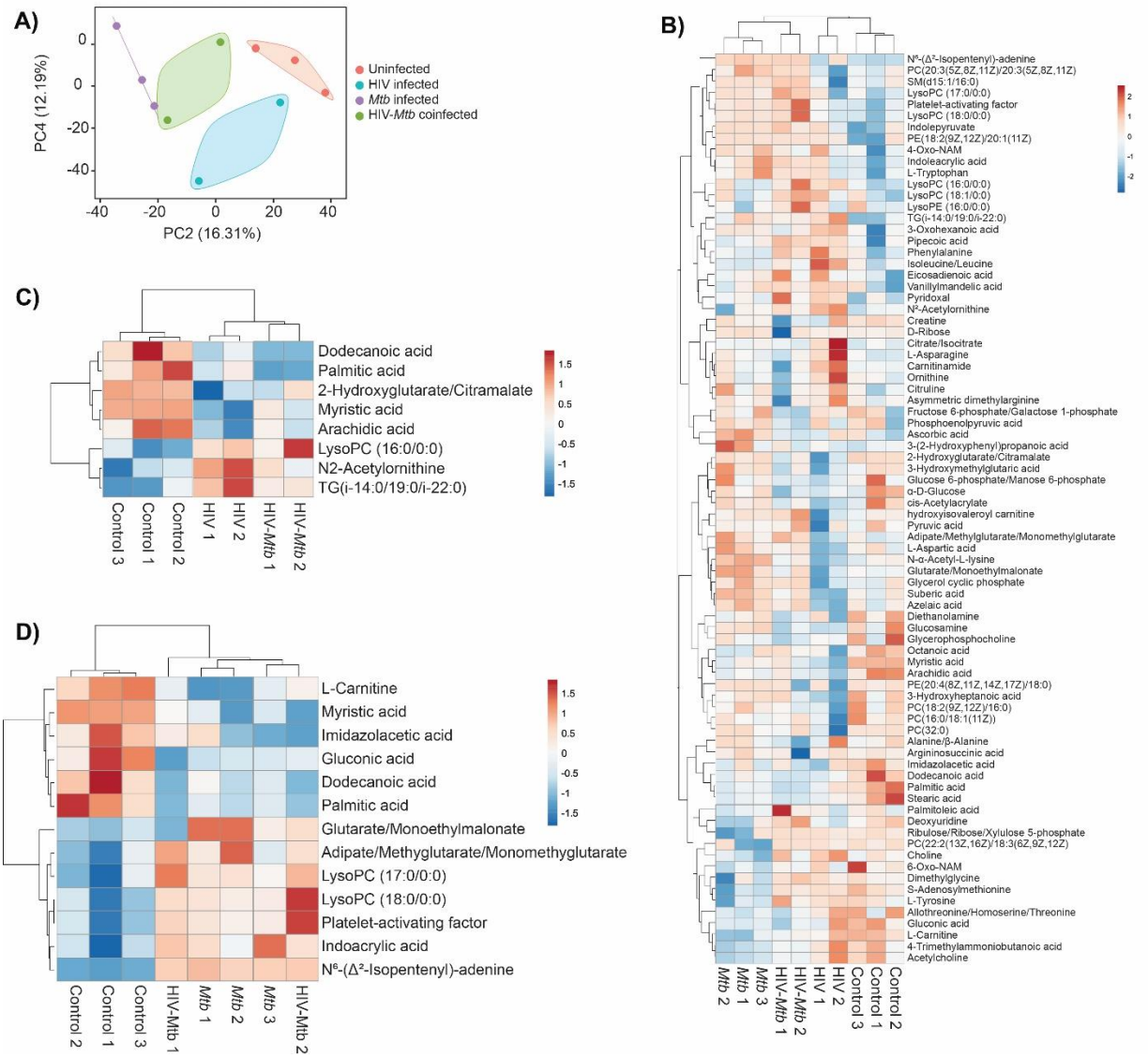

617

618

619 **Figure 7.**

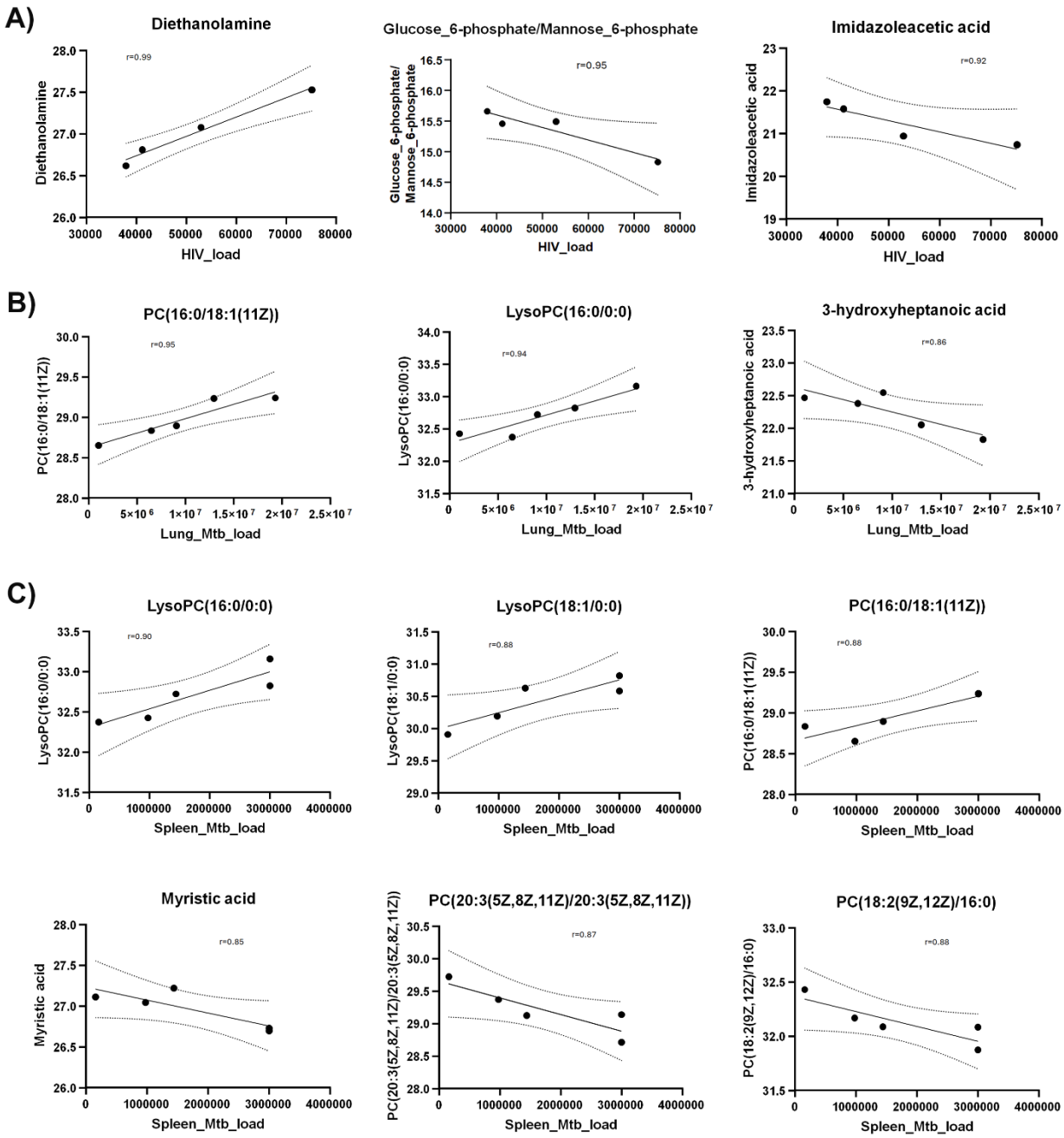

620

621

Table 1: Metabolites differentially abundant in HIV infection.

	Control_1	Control_2	Control_3	HIV_1	HIV_2	HIV.Mtb_1	HIV.Mtb_2	Log2FC	P Values
Dodecanoic acid	30.84885	29.48828	29.18148	27.5704	28.27857	27.25359	27.25838	-2.2493	0.030561
Myristic acid	27.62307	27.64284	27.60289	26.46469	26.14845	27.22307	26.72852	-0.98175	0.022716
Arachidic acid	26.34177	26.28904	25.58546	25.05928	24.64442	25.58284	25.14256	-0.96481	0.033856
Palmitic acid	32.91019	33.14279	32.61936	32.21672	32.58976	31.93621	31.97329	-0.71178	0.022067
2-Hydroxyglutarate/Citramalate	25.06593	25.04706	25.11372	24.06289	24.50181	24.48949	24.90492	-0.58579	0.04128
N2-Acetylornithine	21.69086	21.75382	21.41989	22.18159	22.33382	22.04002	21.82825	0.474396	0.024962
LysoPC(16:0/0:0)	32.25447	32.3347	32.58121	32.82015	32.90289	32.72403	33.16134	0.511976	0.014624
TG(i-14:0/19:0/i-22:0)	26.03645	26.48443	26.03211	26.84162	27.13346	26.63223	26.67844	0.637108	0.02702

Table 2: Metabolites differentially abundant in Mtb infection

	Control_1	Control_2	Control_3	Mtb_1	Mtb_2	Mtb_3	HIV.Mtb_1	HIV.Mtb_2	Log2FC	P Values
Dodecanoic acid	30.84885	29.48828	29.18148	28.63719	27.70525	28.08153	27.25359	27.25838	-2.05235	0.036073
L-Carnitine	29.48852	29.10614	29.56318	27.76163	27.77312	28.5133	28.5302	28.77454	-1.11539	0.004612
Gluconic acid	27.48128	26.69745	27.25191	26.19547	26.24986	26.29529	25.81699	26.40603	-0.95082	0.038034
Palmitic acid	32.91019	33.14279	32.61936	32.25708	32.07672	32.22627	31.93621	31.97329	-0.79686	0.020473
Myristic acid	27.62307	27.64284	27.60289	27.11416	26.69864	27.04336	27.22307	26.72852	-0.66138	0.003101
Imidazoleacetic acid	22.10264	21.58731	21.79266	21.68153	21.05739	20.98498	21.58037	20.94255	-0.57817	0.040855
Glutarate/Monoethylmalonate	23.40639	23.4395	23.50502	23.97748	23.97929	23.69304	23.38075	23.76985	0.309782	0.046714
Adipate/Methyglutarate/ Monomethylglutarate	22.09507	22.23793	22.42262	22.54096	22.81072	22.38233	22.71625	22.58343	0.354862	0.037601
Indoleacrylic acid	25.11462	25.54944	25.52602	25.9564	25.74232	26.24451	26.02944	25.90877	0.579597	0.031357
LysoPC(18:0/0:0)	30.93056	31.40324	31.21889	31.77792	31.69742	31.71439	31.8485	32.31356	0.68613	0.014163
Platelet-activating factor	30.90966	31.38026	31.20963	31.7655	31.68164	31.70822	31.88227	32.29686	0.70038	0.013158
LysoPC(17:0/0:0)	26.47687	26.82401	27.24183	27.52935	27.56634	27.37764	27.9864	27.78227	0.80083	0.048066
N6-(delta2-Isopentenyl)-adenine	-20.6891	-18.9004	-18.5067	10.33699	7.60551	8.233653	8.368181	8.958558	28.06597	5.36E-06

627 **References**

628 1. WHO *Global Tuberculosis Report*; WHO: Geneva, Switzerland, 2023, 2023.
629 2. Palanivel, J.; Sounderrajan, V.; Thangam, T.; Rao, S. S.; Harshavardhan, S.;
630 Parthasarathy, K., Latent Tuberculosis: Challenges in Diagnosis and Treatment, Perspectives, and
631 the Crucial Role of Biomarkers. *Curr Microbiol* **2023,** *80* (12), 392.
632 3. Kaushal, D.; Singh, D. K.; Mehra, S., Immune Responses in Lung Granulomas during
633 Mtb/HIV Co-Infection: Implications for Pathogenesis and Therapy. *Pathogens* **2023,** *12* (9).
634 4. WHO, HIV and AIDS factsheet. WHO, Ed. Geneva, Switzerland, 2023.
635 5. Azevedo-Pereira, J. M.; Pires, D.; Calado, M.; Mandal, M.; Santos-Costa, Q.; Anes, E.,
636 HIV/Mtb Co-Infection: From the Amplification of Disease Pathogenesis to an "Emerging
637 Syndemic".
638 6. WHO *Global Tuberculosis Report*; WHO: Geneva, Switzerland, 2020.
639 7. Sharan, R.; Bucşan, A. N.; Ganatra, S.; Paiardini, M.; Mohan, M.; Mehra, S.; Khader,
640 S. A.; Kaushal, D., Chronic Immune Activation in TB/HIV Co-infection. *Trends in Microbiology*
641 **2020,** *28* (8), 619-632.
642 8. Estes, J. D.; Wong, S. W.; Brenchley, J. M., Nonhuman primate models of human viral
643 infections. *Nature Reviews Immunology* **2018,** *18* (6), 390-404.
644 9. Okoye, A. A.; Picker, L. J., <scp>CD</scp>4⁺ T-cell depletion in
645 <scp>HIV</scp> infection: mechanisms of immunological failure. *Immunological Reviews*
646 **2013,** *254* (1), 54-64.
647 10. Hunter, R. L.; Actor, J. K.; Hwang, S. A.; Khan, A.; Urbanowski, M. E.; Kaushal, D.;
648 Jagannath, C., Pathogenesis and Animal Models of Post-Primary (Bronchogenic) Tuberculosis, A
649 Review. *Pathogens* **2018,** *7* (1).
650 11. Kaushal, D.; Mehra, S.; Didier, P. J.; Lackner, A. A., The non-human primate model of
651 tuberculosis. *J Med Primatol* **2012,** *41* (3), 191-201.
652 12. Cepeda, M.; Salas, M.; Folwarczny, J.; Leandro, A. C.; Hodara, V. L.; de la Garza, M.
653 A.; Dick, E. J., Jr.; Owston, M.; Armitige, L. Y.; Gauduin, M. C., Establishment of a neonatal
654 rhesus macaque model to study Mycobacterium tuberculosis infection. *Tuberculosis (Edinb)*
655 **2013,** *93 Suppl*, S51-9.
656 13. Ganatra, S. R.; Bucsan, A. N.; Alvarez, X.; Kumar, S.; Chatterjee, A.; Quezada, M.;
657 Fish, A.; Singh, D. K.; Singh, B.; Sharan, R.; Lee, T. H.; Shanmugasundaram, U.; Velu, V.;
658 Khader, S. A.; Mehra, S.; Rengarajan, J.; Kaushal, D., Antiretroviral therapy does not reduce
659 tuberculosis reactivation in a tuberculosis-HIV coinfection model. *J Clin Invest* **2020,** *130* (10),
660 5171-5179.
661 14. Lepard, M.; Yang, J. X.; Afkhami, S.; Nazli, A.; Zganiacz, A.; Tang, S.; Choi, M. W.
662 Y.; Vahedi, F.; Deshiere, A.; Tremblay, M. J.; Xing, Z.; Kaushic, C.; Gillgrass, A., Comparing
663 Current and Next-Generation Humanized Mouse Models for Advancing HIV and HIV/Mtb Co-
664 Infection Studies. *Viruses* **2022,** *14* (9), 1927.
665 15. Nusbaum, R. J.; Calderon, V. E.; Huante, M. B.; Sutjita, P.; Vijayakumar, S.;
666 Lancaster, K. L.; Hunter, R. L.; Actor, J. K.; Cirillo, J. D.; Aronson, J.; Gelman, B. B.;
667 Lisinicchia, J. G.; Valbuena, G.; Endsley, J. J., Pulmonary Tuberculosis in Humanized Mice
668 Infected with HIV-1. *Scientific Reports* **2016,** *6* (1), 21522.
669 16. Hunter, R.; Actor, J.; Hwang, S.-A.; Khan, A.; Urbanowski, M.; Kaushal, D.;
670 Jagannath, C., Pathogenesis and Animal Models of Post-Primary (Bronchogenic) Tuberculosis, A
671 Review. *Pathogens* **2018,** *7* (1), 19.

17. Hunter, R. L.; Olsen, M.; Jagannath, C.; Actor, J. K., Trehalose 6,6′-Dimycolate and Lipid in the Pathogenesis of Caseating Granulomas of Tuberculosis in Mice. *The American Journal of Pathology* **2006,** *168* (4), 1249-1261.
18. Calderon, V. E.; Valbuena, G.; Goez, Y.; Judy, B. M.; Huante, M. B.; Sutjita, P.; Johnston, R. K.; Estes, D. M.; Hunter, R. L.; Actor, J. K.; Cirillo, J. D.; Endsley, J. J., A Humanized Mouse Model of Tuberculosis. *PLoS ONE* **2013,** *8* (5), e63331.
19. Biradar, S.; Agarwal, Y.; Lotze, M. T.; Bility, M. T.; Mailliard, R. B., The BLT Humanized Mouse Model as a Tool for Studying Human Gamma Delta T Cell-HIV Interactions In Vivo. *Frontiers in Immunology* **2022,** *13*.
20. Denton, P. W.; Garcia, J. V., Humanized mouse models of HIV infection. *AIDS Rev* **2011,** *13* (3), 135-48.
21. Victor Garcia, J., Humanized mice for HIV and AIDS research. *Current Opinion in Virology* **2016,** *19*, 56-64.
22. Huante, M. B.; Saito, T. B.; Nusbaum, R. J.; Naqvi, K. F.; Chauhan, S.; Hunter, R. L.; Actor, J. K.; Rudra, J. S.; Endsley, M. A.; Lisinicchia, J. G.; Gelman, B. B.; Endsley, J. J., Small Animal Model of Post-chemotherapy Tuberculosis Relapse in the Setting of HIV Co-infection. *Frontiers in Cellular and Infection Microbiology* **2020,** *10*.
23. Lang, J.; Kelly, M.; Freed, B. M.; McCarter, M. D.; Kedl, R. M.; Torres, R. M.; Pelanda, R., Studies of Lymphocyte Reconstitution in a Humanized Mouse Model Reveal a Requirement of T Cells for Human B Cell Maturation. *The Journal of Immunology* **2013,** *190* (5), 2090-2101.
24. Chen, Q.; He, F.; Kwang, J.; Chan, J. K. Y.; Chen, J., GM-CSF and IL-4 Stimulate Antibody Responses in Humanized Mice by Promoting T, B, and Dendritic Cell Maturation. *The Journal of Immunology* **2012,** *189* (11), 5223-5229.
25. Yu, C. I.; Martinek, J.; Wu, T. C.; Kim, K. I.; George, J.; Ahmadzadeh, E.; Maser, R.; Marches, F.; Metang, P.; Authie, P.; Oliveira, V. K. P.; Wang, V. G.; Chuang, J. H.; Robson, P.; Banchereau, J.; Palucka, K., Human KIT+ myeloid cells facilitate visceral metastasis by melanoma. *J Exp Med* **2021,** *218* (6).
26. Coughlan, A. M.; Harmon, C.; Whelan, S.; O'Brien, E. C.; O'Reilly, V. P.; Crotty, P.; Kelly, P.; Ryan, M.; Hickey, F. B.; O'Farrelly, C.; Little, M. A., Myeloid Engraftment in Humanized Mice: Impact of Granulocyte-Colony Stimulating Factor Treatment and Transgenic Mouse Strain. *Stem Cells Dev* **2016,** *25* (7), 530-41.
27. Billerbeck, E.; Barry, W. T.; Mu, K.; Dorner, M.; Rice, C. M.; Ploss, A., Development of human CD4+FoxP3+ regulatory T cells in human stem cell factor-, granulocyte-macrophage colony-stimulating factor-, and interleukin-3-expressing NOD-SCID IL2Rgamma(null) humanized mice. *Blood* **2011,** *117* (11), 3076-86.
28. Janke, L. J.; Imai, D. M.; Tillman, H.; Doty, R.; Hoenerhoff, M. J.; Xu, J. J.; Freeman, Z. T.; Allen, P.; Fowlkes, N. W.; Iacobucci, I.; Dickerson, K.; Mullighan, C. G.; Vogel, P.; Rehg, J. E., Development of Mast Cell and Eosinophil Hyperplasia and HLH/MAS-Like Disease in NSG-SGM3 Mice Receiving Human CD34+ Hematopoietic Stem Cells or Patient-Derived Leukemia Xenografts. *Vet Pathol* **2021,** *58* (1), 181-204.
29. Terahara, K.; Iwabuchi, R.; Tsunetsugu-Yokota, Y., Perspectives on Non-BLT Humanized Mouse Models for Studying HIV Pathogenesis and Therapy. *Viruses* **2021,** *13* (5).
30. Wang, X.; Barnes, P. F.; Huang, F.; Alvarez, I. B.; Neuenschwander, P. F.; Sherman, D. R.; Samten, B., Early Secreted Antigenic Target of 6-kDa Protein of <i>Mycobacterium

717 tuberculosis Primes Dendritic Cells To Stimulate Th17 and Inhibit Th1 Immune Responses.
718 *The Journal of Immunology* **2012,** *189* (6), 3092-3103.
719 31. van 't Wout, A. B.; Schuitemaker, H.; Kootstra, N. A., Isolation and propagation of HIV-1
720 on peripheral blood mononuclear cells. *Nat Protoc* **2008,** *3* (3), 363-70.
721 32. Feng, Y.; Kong, Y.; Barnes, P. F.; Huang, F.-F.; Klucar, P.; Wang, X.; Samten, B.;
722 Sengupta, M.; Machona, B.; Donis, R.; Tvinnereim, A. R.; Shams, H., Exposure to Cigarette
723 Smoke Inhibits the Pulmonary T-Cell Response to Influenza Virus andMycobacterium
724 tuberculosis. *Infection and Immunity* **2011,** *79* (1), 229-237.
725 33. Moreira, J. D.; Iakhiaev, A.; Vankayalapati, R.; Jung, B.-G.; Samten, B., Histone
726 deacetylase-2 controls IL-1β production through the regulation of NLRP3 expression and
727 activation in tuberculosis infection. *iScience* **2022,** *25* (8), 104799.
728 34. Morton, J.; Snider, T. A., Guidelines for collection and processing of lungs from aged
729 mice for histological studies. *Pathobiology of Aging & Age-related Diseases* **2017,** *7* (1),
730 1313676.
731 35. Davenport, M. L.; Sherrill, T. P.; Blackwell, T. S.; Edmonds, M. D., Perfusion and
732 Inflation of the Mouse Lung for Tumor Histology. *J Vis Exp* **2020,** (162).
733 36. Tucker, T. A.; Jeffers, A.; Alvarez, A.; Owens, S.; Koenig, K.; Quaid, B.; Komissarov,
734 A. A.; Florova, G.; Kothari, H.; Pendurthi, U.; Mohan Rao, L. V.; Idell, S., Plasminogen
735 Activator Inhibitor-1 Deficiency Augments Visceral Mesothelial Organization, Intrapleural
736 Coagulation, and Lung Restriction in Mice with Carbon Black/Bleomycin–Induced Pleural
737 Injury. *American Journal of Respiratory Cell and Molecular Biology* **2014,** *50* (2), 316-327.
738 37. Butler, S. L.; Hansen, M. S. T.; Bushman, F. D., A quantitative assay for HIV DNA
739 integration in vivo. *Nature Medicine* **2001,** *7* (5), 631-634.
740 38. Zaqout, S.; Becker, L.-L.; Kaindl, A. M., Immunofluorescence Staining of Paraffin
741 Sections Step by Step. *Frontiers in Neuroanatomy* **2020,** *14*.
742 39. Yang, B.; Mukherjee, T.; Radhakrishnan, R.; Paidipally, P.; Ansari, D.; John, S.;
743 Vankayalapati, R.; Tripathi, D.; Yi, G., HIV-Differentiated Metabolite N-Acetyl-L-Alanine
744 Dysregulates Human Natural Killer Cell Responses to Mycobacterium tuberculosis Infection.
745 *International Journal of Molecular Sciences* **2023,** *24* (8), 7267.
746 40. Ritchie, M. E.; Phipson, B.; Wu, D.; Hu, Y.; Law, C. W.; Shi, W.; Smyth, G. K., limma
747 powers differential expression analyses for RNA-sequencing and microarray studies. *Nucleic
748 Acids Research* **2015,** *43* (7), e47-e47.
749 41. Chackerian, A. A.; Alt, J. M.; Perera, T. V.; Dascher, C. C.; Behar, S. M., Dissemination
750 ofMycobacterium tuberculosisIs Influenced by Host Factors and Precedes the Initiation
751 of T-Cell Immunity. *Infection and Immunity* **2002,** *70* (8), 4501-4509.
752 42. Domínguez-Oliva, A.; Hernández-Ávalos, I.; Martínez-Burnes, J.; Olmos-Hernández,
753 A.; Verduzco-Mendoza, A.; Mota-Rojas, D., The Importance of Animal Models in Biomedical
754 Research: Current Insights and Applications. *Animals* **2023,** *13* (7), 1223.
755 43. Mukherjee, P.; Roy, S.; Ghosh, D.; Nandi, S. K., Role of animal models in biomedical
756 research: a review. *Laboratory Animal Research* **2022,** *38* (1).
757 44. Rong, N.; Liu, J., Development of animal models for emerging infectious diseases by
758 breaking the barrier of species susceptibility to human pathogens. *Emerging Microbes &
759 Infections* **2023,** *12* (1).
760 45. Gao, F.; Bailes, E.; Robertson, D. L.; Chen, Y.; Rodenburg, C. M.; Michael, S. F.;
761 Cummins, L. B.; Arthur, L. O.; Peeters, M.; Shaw, G. M.; Sharp, P. M.; Hahn, B. H., Origin of
762 HIV-1 in the chimpanzee Pan troglodytes troglodytes. *Nature* **1999,** *397* (6718), 436-441.

763 46. Nakayama, E. E.; Shioda, T., TRIM5α and Species Tropism of HIV/SIV. *Frontiers in*
764 *Microbiology* **2012,** *3*.
765 47. Brehm, M. A.; Cuthbert, A.; Yang, C.; Miller, D. M.; Diiorio, P.; Laning, J.;
766 Burzenski, L.; Gott, B.; Foreman, O.; Kavirayani, A.; Herlihy, M.; Rossini, A. A.; Shultz, L.
767 D.; Greiner, D. L., Parameters for establishing humanized mouse models to study human
768 immunity: Analysis of human hematopoietic stem cell engraftment in three immunodeficient
769 strains of mice bearing the IL2rγnull mutation. *Clinical Immunology* **2010,** *135* (1), 84-98.
770 48. Martínez-Sanz, J.; Díaz-Álvarez, J.; Rosas Cancio-Suarez, M.; Ron, R.; Iribarren, J. A.;
771 Bernal, E.; Gutiérrez, F.; Ruiz Sancho, A.; Cabello, N.; Olalla, J.; Moreno, S.; Serrano-Villar,
772 S.; CoRIS, Expanding HIV clinical monitoring: the role of CD4, CD8, and CD4/CD8 ratio in
773 predicting non-AIDS events. *eBioMedicine* **2023,** *95*, 104773.
774 49. Serrano-Villar, S.; Sainz, T.; Lee, S. A.; Hunt, P. W.; Sinclair, E.; Shacklett, B. L.;
775 Ferre, A. L.; Hayes, T. L.; Somsouk, M.; Hsue, P. Y.; Van Natta, M. L.; Meinert, C. L.;
776 Lederman, M. M.; Hatano, H.; Jain, V.; Huang, Y.; Hecht, F. M.; Martin, J. N.; Mccune, J.
777 M.; Moreno, S.; Deeks, S. G., HIV-Infected Individuals with Low CD4/CD8 Ratio despite
778 Effective Antiretroviral Therapy Exhibit Altered T Cell Subsets, Heightened CD8+ T Cell
779 Activation, and Increased Risk of Non-AIDS Morbidity and Mortality. *PLoS Pathogens* **2014,** *10*
780 (5), e1004078.
781 50. Mikulak, J.; Di Vito, C.; Zaghi, E.; Mavilio, D., Host Immune Responses in HIV-1
782 Infection: The Emerging Pathogenic Role of Siglecs and Their Clinical Correlates. *Frontiers in*
783 *Immunology* **2017,** *8*.
784 51. Thoulouze, M. I.; Sol-Foulon, N.; Blanchet, F.; Dautry-Varsat, A.; Schwartz, O.;
785 Alcover, A., Human Immunodeficiency Virus Type-1 Infection Impairs the Formation of the
786 Immunological Synapse. *Immunity* **2006,** *24* (5), 547-561.
787 52. Cao, S.; Li, J.; Lu, J.; Zhong, R.; Zhong, H., Mycobacterium tuberculosis antigens
788 repress Th1 immune response suppression and promotes lung cancer metastasis through PD-
789 1/PDl-1 signaling pathway. *Cell Death & Disease* **2019,** *10* (2).
790 53. McCaffrey, E. F.; Donato, M.; Keren, L.; Chen, Z.; Delmastro, A.; Fitzpatrick, M. B.;
791 Gupta, S.; Greenwald, N. F.; Baranski, A.; Graf, W.; Kumar, R.; Bosse, M.; Fullaway, C. C.;
792 Ramdial, P. K.; Forgó, E.; Jojic, V.; Van Valen, D.; Mehra, S.; Khader, S. A.; Bendall, S. C.;
793 Van De Rijn, M.; Kalman, D.; Kaushal, D.; Hunter, R. L.; Banaei, N.; Steyn, A. J. C.; Khatri,
794 P.; Angelo, M., The immunoregulatory landscape of human tuberculosis granulomas. *Nature*
795 *Immunology* **2022,** *23* (2), 318-329.
796 54. Kruize, Z.; Kootstra, N. A., The Role of Macrophages in HIV-1 Persistence and
797 Pathogenesis. *Frontiers in Microbiology* **2019,** *10*.
798 55. Lerner, T. R.; Borel, S.; Greenwood, D. J.; Repnik, U.; Russell, M. R. G.; Herbst, S.;
799 Jones, M. L.; Collinson, L. M.; Griffiths, G.; Gutierrez, M. G., Mycobacterium
800 tuberculosis replicates within necrotic human macrophages. *Journal of Cell Biology* **2017,**
801 *216* (3), 583-594.
802 56. Cronan, M. R., In the Thick of It: Formation of the Tuberculous Granuloma and Its
803 Effects on Host and Therapeutic Responses. *Frontiers in Immunology* **2022,** *13*.
804 57. Lin, Y.; Gong, J.; Zhang, M.; Xue, W.; Barnes, P. F., Production of Monocyte
805 Chemoattractant Protein 1 in Tuberculosis Patients. *Infection and Immunity* **1998,** *66* (5), 2319-
806 2322.
807 58. Mishra, A.; Singh, V. K.; Actor, J. K.; Hunter, R. L.; Jagannath, C.; Subbian, S.; Khan,
808 A., GM-CSF Dependent Differential Control of Mycobacterium tuberculosis Infection in Human

809 and Mouse Macrophages: Is Macrophage Source of GM-CSF Critical to Tuberculosis Immunity?
810 *Frontiers in Immunology* **2020,** *11*.
811 59. Robinson, R. T., T Cell Production of GM-CSF Protects the Host during Experimental
812 Tuberculosis. *mBio* **2017,** *8* (6), e02087-17.
813 60. Luo, J.; Zhang, M.; Yan, B.; Li, F.; Guan, S.; Chang, K.; Jiang, W.; Xu, H.; Yuan, T.;
814 Chen, M.; Deng, S., Diagnostic performance of plasma cytokine biosignature combination and
815 MCP-1 as individual biomarkers for differentiating stages Mycobacterium tuberculosis infection.
816 *J Infect* **2019,** *78* (4), 281-291.
817 61. Hilda, J. N.; Narasimhan, M.; Das, S. D., Neutrophils from pulmonary tuberculosis
818 patients show augmented levels of chemokines MIP-1α, IL-8 and MCP-1 which further increase
819 upon in vitro infection with mycobacterial strains. *Hum Immunol* **2014,** *75* (8), 914-22.
820 62. Saukkonen, J. J.; Bazydlo, B.; Thomas, M.; Strieter, R. M.; Keane, J.; Kornfeld, H., β-
821 Chemokines Are Induced byMycobacterium tuberculosisand Inhibit Its Growth. *Infection*
822 *and Immunity* **2002,** *70* (4), 1684-1693.
823 63. Almeida, A. S.; Lago, P. C. M.; Boechat, N.; Huard, R. C.; Lazzarini, L. C. O.; Santos,
824 A. R.; Nociari, M.; Zhu, H.; Perez-Sweeney, B. M.; Bang, H.; Ni, Q.; Huang, J.; Gibson, A.
825 L.; Flores, V. C.; Pecanha, L. R.; Kritski, A. N. L.; Lapa E Silva, J. R.; Ho, J. L., Tuberculosis
826 Is Associated with a Down-Modulatory Lung Immune Response That Impairs Th1-Type
827 Immunity. *The Journal of Immunology* **2009,** *183* (1), 718-731.
828 64. Gern, B. H.; Adams, K. N.; Plumlee, C. R.; Stoltzfus, C. R.; Shehata, L.; Moguche, A.
829 O.; Busman-Sahay, K.; Hansen, S. G.; Axthelm, M. K.; Picker, L. J.; Estes, J. D.; Urdahl, K.
830 B.; Gerner, M. Y., TGFβ restricts expansion, survival, and function of T cells within the
831 tuberculous granuloma. *Cell Host & Microbe* **2021,** *29* (4), 594-606.e6.
832 65. Knaul, J. K.; Jörg, S.; Oberbeck-Mueller, D.; Heinemann, E.; Scheuermann, L.;
833 Brinkmann, V.; Mollenkopf, H.-J.; Yeremeev, V.; Kaufmann, S. H. E.; Dorhoi, A., Lung-
834 Residing Myeloid-derived Suppressors Display Dual Functionality in Murine Pulmonary
835 Tuberculosis. *American Journal of Respiratory and Critical Care Medicine* **2014,** *190* (9), 1053-
836 1066.
837 66. Gerson, K. D.; Yang, N.; Anton, L.; Levy, M.; Ravel, J.; Elovitz, M. A.; Burris, H. H.,
838 Second trimester short cervix is associated with decreased abundance of cervicovaginal lipid
839 metabolites. *American Journal of Obstetrics and Gynecology* **2022,** *227* (2), 273.e1-273.e18.
840 67. Prell, G. D.; Martinelli, G. P.; Holstein, G. R.; Matulić-Adamić, J.; Watanabe, K. A.;
841 Chan, S. L. F.; Morgan, N. G.; Haxhiu, M. A.; Ernsberger, P., Imidazoleacetic acid-ribotide: An
842 endogenous ligand that stimulates imidazol(in)e receptors. *Proceedings of the National Academy*
843 *of Sciences* **2004,** *101* (37), 13677-13682.
844 68. Pedersen, M.; Nielsen, C. M.; Permin, H., HIV antigen-induced release of histamine
845 from basophils from HIV infected patients. *Allergy* **1991,** *46* (3), 206-212.
846 69. Grunfeld, C.; Kotler, D. P.; Hamadeh, R.; Tierney, A.; Wang, J.; Pierson, R. N.,
847 Hypertriglyceridemia in the acquired immunodeficiency syndrome. *The American Journal of*
848 *Medicine* **1989,** *86* (1), 27-31.
849 70. Zhang, J.; Jin, H.-L.; Jian, F.-B.; Feng, S.-L.; Zhu, W.-T.; Li, L.-H.; Yuan, Z.-W.,
850 Evaluation of lipid metabolism imbalance in HIV-infected patients with metabolic disorders
851 using high-performance liquid chromatography-tandem mass spectrometry. *Clinica Chimica*
852 *Acta* **2022,** *526*, 30-42.
853 71. Bowman, E. R.; Kulkarni, M.; Gabriel, J.; Mo, X.; Klamer, B.; Belury, M.; Lake, J.
854 E.; Zidar, D.; Sieg, S. F.; Mehta, N. N.; Playford, M. P.; Kuritzkes, D. R.; Andrade, A.;

Schmidt, E. K.; Taylor, C.; Overton, E. T.; Willig, A. L.; Lederman, M. M.; Funderburg, N. T., Plasma lipidome abnormalities in people with HIV initiating antiretroviral therapy. *Translational Medicine Communications* **2020,** *5* (1).

72. Ganguly, S.; Vithlani, V. V.; Kesharwani, A. K.; Kuhu, R.; Baskar, L.; Mitramazumder, P.; Sharon, A.; Dev, A., Synthesis, antibacterial and potential anti-HIV activity of some novel imidazole analogs. *Acta Pharm* **2011,** *61* (2), 187-201.

73. Abdel-Meguid, S. S.; Metcalf, B. W.; Carr, T. J.; Demarsh, P.; DesJarlais, R. L.; Fisher, S.; Green, D. W.; Ivanoff, L.; Lambert, D. M.; Murthy, K. H.; et al., An orally bioavailable HIV-1 protease inhibitor containing an imidazole-derived peptide bond replacement: crystallographic and pharmacokinetic analysis. *Biochemistry* **1994,** *33* (39), 11671-7.

74. Loisel-Meyer, S.; Swainson, L.; Craveiro, M.; Oburoglu, L.; Mongellaz, C.; Costa, C.; Martinez, M.; Cosset, F. L.; Battini, J. L.; Herzenberg, L. A.; Herzenberg, L. A.; Atkuri, K. R.; Sitbon, M.; Kinet, S.; Verhoeyen, E.; Taylor, N., Glut1-mediated glucose transport regulates HIV infection. *Proc Natl Acad Sci U S A* **2012,** *109* (7), 2549-54.

75. Hollenbaugh, J. A.; Munger, J.; Kim, B., Metabolite profiles of human immunodeficiency virus infected CD4+ T cells and macrophages using LC-MS/MS analysis. *Virology* **2011,** *415* (2), 153-9.

76. Kirwan, D. E.; Chong, D. L. W.; Friedland, J. S., Platelet Activation and the Immune Response to Tuberculosis. *Frontiers in Immunology* **2021,** *12*.

77. Samanovic, M. I.; Tu, S.; Novák, O.; Iyer, L. M.; McAllister, F. E.; Aravind, L.; Gygi, S. P.; Hubbard, S. R.; Miroslav, S.; Darwin, K. H., Proteasomal Control of Cytokinin Synthesis Protects Mycobacterium tuberculosis against Nitric Oxide. *Molecular Cell* **2015,** *57* (6), 984-994.

78. Yano, H.; Oyanagi, E.; Kato, Y.; Samejima, Y.; Sasaki, J.; Utsumi, K., l-Carnitine is essential to β-oxidation of quarried fatty acid from mitochondrial membrane by PLA2. *Molecular and Cellular Biochemistry* **2010,** *342* (1-2), 95-100.

79. Herbert, C.; Luies, L.; Loots, D. T.; Williams, A. A., The metabolic consequences of HIV/TB co-infection. *BMC Infectious Diseases* **2023,** *23* (1).

80. Cumming, B. M.; Addicott, K. W.; Adamson, J. H.; Steyn, A. J., Mycobacterium tuberculosis induces decelerated bioenergetic metabolism in human macrophages. *eLife* **2018,** *7*.

81. Daniel, J.; Maamar, H.; Deb, C.; Sirakova, T. D.; Kolattukudy, P. E., Mycobacterium tuberculosis Uses Host Triacylglycerol to Accumulate Lipid Droplets and Acquires a Dormancy-Like Phenotype in Lipid-Loaded Macrophages. *PLoS Pathogens* **2011,** *7* (6), e1002093.